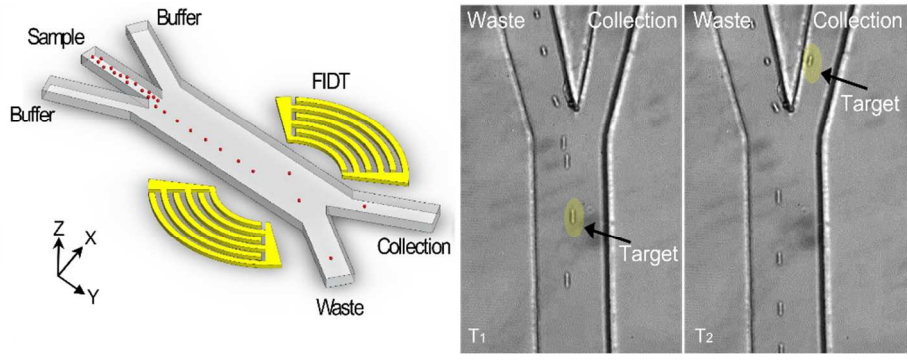




A high-throughput standing surface acoustic wave (SSAW)-based cell sorter

Journal:	<i>Lab on a Chip</i>
Manuscript ID:	LC-ART-06-2015-000706.R1
Article Type:	Paper
Date Submitted by the Author:	01-Aug-2015
Complete List of Authors:	<p>Ren, Liqiang; The Pennsylvania State University, Department of Engineering Science and Mechanics Chen, Yuchao; The Pennsylvania State University, Department of Engineering Science and Mechanics Li, Peng; The Pennsylvania State University, Department of Engineering Science and Mechanics Mao, Zhangming; The Pennsylvania State University, Department of Engineering Science and Mechanics Huang, Po-Hsun; The Pennsylvania State University, Department of Engineering Science and Mechanics Rufo, Joseph; The Pennsylvania State University, Department of Engineering Science and Mechanics Guo, Feng; The Pennsylvania State University, Department of Engineering Science and Mechanics Wang, Lin; Ascent Bio-Nano Technologies Inc., McCoy, J. Philip; National Heart, Lung, and Blood Institute, Levine, Stewart; National Institute of Health, Laboratory of Asthma and Lung Inflammation Huang, Tony Jun; The Pennsylvania State University, Department of Engineering Science and Mechanics</p>

We developed a standing surface acoustic wave (SSAW)-based cell sorting device. The throughput of our device has been significantly improved by using focused interdigital transducers (FIDTs) as SSAW generator.



A high-throughput standing surface acoustic wave (SSAW)-based cell sorter

Liqiang Ren,^{†a} Yuchao Chen,^{†a} Peng Li,^a Zhangming Mao,^a Po-Hsun Huang,^a Joseph Rufo,^a Feng Guo,^a Lin Wang,^b J. Philip McCoy,^c Stewart J. Levine^c and Tony Jun Huang^{*a}

⁵ Received (in XXX, XXX) Xth XXXXXXXXX 20XX, Accepted Xth XXXXXXXXX 20XX

First published on the web Xth XXXXXXXXX 20XX

DOI:

Acoustic-based fluorescence activated cell sorters (FACS) have drawn increased attention in recent years due to their versatility, high biocompatibility, high controllability, and simple design.

¹⁰ However, the sorting throughput for existing acoustic cell sorters is far from optimum for practical applications. Here we report a high-throughput cell sorting method based on standing surface acoustic wave (SSAW). We utilized a pair of focused interdigital transducers (FIDTs) to generate SSAW with high resolution and high energy efficiency. As a result, the sorting throughput is improved significantly from conventional acoustic-based cell sorting methods. We demonstrated ¹⁵ the successful sorting of 10 μm polystyrene particles with a minimum actuation time of 72 μs , which translates to a potential sorting rate of more than 13,800 events/s. Without using a cell-detection unit, we were able to demonstrate an actual sorting throughput of 3,300 events/s. Our sorting method can be conveniently integrated with upstream detection units, and it represents an important development towards a functional acoustic-based FACS system.

²⁰ Introduction

Sorting individual cells/particles of interest from a heterogeneous population has been of critical importance in biological studies and clinical applications, such as single cell sequencing, rare cell isolation, and drug screening.^{1,2} Over the ²⁵ past 40 years, these tasks have mainly been achieved by commercial fluorescence activated cell sorters (FACS).^{3,4} Despite the wide adoption of commercial FACS, many applications require sorting systems that can provide better biocompatibility (*i.e.*, the ability to maintain cell integrity ³⁰ during the cell-sorting process) and biosafety while maintaining high purity and high yield.

In the past decade, microfluidics has emerged as a powerful tool for manipulating cells, and many microfluidic-based cell sorting methods have been developed to improve ³⁵ conventional FACS. Previously demonstrated microfluidic techniques of cell manipulation have relied on a variety of underlying mechanisms, including dielectrophoresis,⁵⁻⁷ optical tweezers,⁸⁻¹¹ magnetic forces,^{12,13} hydrodynamic flows,¹⁴ and valve-based switching.¹⁵ Although these methods are capable ⁴⁰ of sorting cells from low-volume samples, most suffer from drawbacks such as low throughput, bulky instrument, and low biocompatibility. An alternative approach to sort cells in microfluidics is to utilize acoustic forces which have been recently explored for alignment, separation, and enrichment of ⁴⁵ particles and cells.¹⁶⁻²⁸ Compared to other existing sorting methods, acoustic-based sorting methods offers unique advantages such as contactless manipulation, small device footprint, low cost, high controllability, and high biocompatibility. The acoustic intensity and frequency used in ⁵⁰ acoustic-based microfluidic devices are similar to those used in ultrasonic imaging, which has been proven to be extremely safe.^{29,30} For cell sorting, the high compatibility is especially important as the potential damage and alteration of cell properties (such as gene expressions) during the sorting

⁵⁵ process will pose significant difficulties for downstream cell culture and analysis.

So far, both bulk acoustic waves (BAW) and surface acoustic waves (SAW) have been used to realize the cell sorting function inside a closed microfluidic channel. ⁶⁰ However, currently, the major obstacle for the practical applications of acoustic-based cell sorters is the limited throughput. By using BAW, Johansson *et al.* presented the first BAW-based FACS with a sorting rate of 27 cells/s in 2009.³¹ A miniaturized piezoelectric transducer was used to ⁶⁵ generate a standing bulk acoustic wave (SBAW) field in the channel, and the acoustic radiation force acted on a density interface to move the fluid, resulting in the controlled movement of cells. Later, Lee *et al.* used a high-frequency BAW beam to detect and sort particles with a sorting rate of ⁷⁰ 60 particles/s.³² Recently Jakobsson *et al.* combined the BAW-based focusing and sorting functions together to improve the performance of the acoustic FACS.³³ Particles were pre-focused in the fluid by a high-frequency transducer and then sorted to the pressure node using a low-frequency ⁷⁵ transducer. The sorting throughput reached 150 particles/s. Thus far, the throughput of BAW-based cell sorters is still not comparable to the commercial products. For example, the Beckman Coulter Moflo XDP can reach a sorting throughput of more than 70,000 events/s with greater than 99% purity, and the ⁸⁰ Becton Dickinson (BD) FACS Aria II sorter can reach a similar purity at a throughput of 25,000 events/s.³⁴ This discrepancy is mainly due to the low resolution of the acoustic actuation area caused by the relatively large size of the BAW transducers and the diffraction of low-frequency BAW. A large acoustic ⁸⁵ actuation area requires very low cell concentrations to achieve single-cell-level deflection, thereby making it difficult to improve the sorting throughput. In this regard, SAW appears to be a more favorable choice for high-throughput cell sorting because the acoustic actuation area in the fluid can be well ⁹⁰ controlled.^{35,36} Franke *et al.* demonstrated successful cell sorting using travelling surface acoustic waves (TSAW).³⁷ A small

PDMS post is used to couple the TSAW into the microfluidic channel, TSAW induced streaming is then able to deflect cells of interest within the area of the PDMS post. The minimum acoustic actuation time is 330 μs , which translates to a theoretical maximum sorting rate of 3,000 events/s for aqueous droplets.³⁸

Later, standing surface acoustic waves (SSAW) based cell sorter is also reported.³⁹ The advantage of SSAW-based cell sorters is that it has better control for the position of sorted cells⁴⁰. As a result, it can achieve multi-channel (e.g., five-channel) cell sorting. However, the sorting throughput for droplets can only reach ~ 200 events/s with current device setups.⁴¹ Collectively, there is still a large gap to achieve the standard sorting speed ($>10,000$ events/s) of commercial cell sorters.

In this work, we systematically optimize the design parameters of SSAW-based cell sorters in order to meet the practical needs of cell-sorting applications. We exploited the advantages of focused interdigital transducers (FIDTs) to generate SSAW for cell sorting. Compared to the standard interdigital transducers (SIDTs) used in previous SSAW cell sorters,³⁹ FIDTs are able to generate SAW with higher intensities and a narrower beam width.⁴²⁻⁴⁷ A high energy intensity can generate a higher actuation force for cell sorting, while a narrower beam width means a higher sorting resolution. Here we combined the high intensity and high resolution of SAW generated by FIDTs with the excellent controllability of the SSAW manipulation technique, allowing our device to operate at a very high sorting rate while only using a low input power (several mW). A minimum actuation time of 72 μs was achieved for sorting of 10 μm polystyrene particles; to the best of our knowledge, it is the shortest actuation time required among all the existing acoustic-based sorters. The 72 μs actuation time indicates a theoretical maximum throughput of 13,800 events/s. For cell sorting, a minimum sorting time of 144 μs was also demonstrated. Without a cell-detection unit, we were able to demonstrate an actual sorting throughput of 3,300 events/s. We believe the sorting method here represents a major improvement in the field of acoustic-based cell sorters and moves the field closer to practical applications.

Mechanism

The schematic of our high-throughput SSAW-based sorting device is shown in Fig. 1(a), including a microfluidic channel with 3 inlets and 2 outlets and a pair of concentric circular-shaped

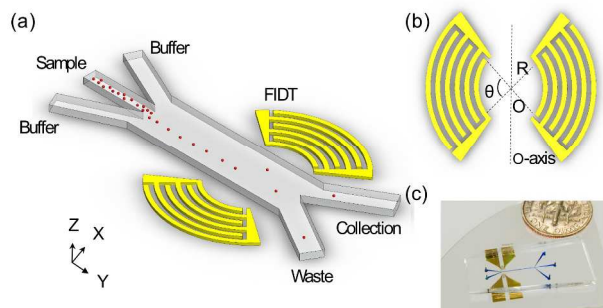


Fig. 1 (a) Schematic of the SSAW-based sorter excited by FIDTs. (b) The concentric geometry of the FIDTs. θ is the degree of arcs and R is the radius of innermost transducer. O is the focal point and the two sets of FIDTs is O-axis symmetric. (c) An optical image of our high-throughput SSAW sorter.

FIDTs. The geometry of the FIDTs is determined by the radius of the innermost IDT finger R and the degree of the circular arc θ as shown in Fig. 1(b). To turn on the sorter, coherent radio frequency (RF) signals are applied to both FIDTs to generate two SAWs propagating in opposite directions. The two SAWs interfere with each other and form SSAW, as well as periodic distribution of pressure nodes and antinodes on the substrate. The SSAW under the microfluidic channel leaks into the liquid medium and creates an acoustic radiation force that drives the suspended particles to the pressure nodes (minimum pressure amplitude) or antinodes (maximum pressure amplitude).⁴⁸ The primary acoustic radiation force acting on any microparticle in a SSAW field can be expressed as^{49,50}

$$F_r = -\left(\frac{\pi p_0^2 V_c \beta_w}{2\lambda}\right) \varphi(\beta, \rho) \sin(2kx) \quad (1)$$

$$\varphi(\beta, \rho) = \frac{5\rho_c - 2\rho_w}{2\rho_c - \rho_w} - \frac{\beta_c}{\beta_w} \quad (2)$$

where p_0 , λ , V_c , ρ_c , ρ_w , β_c and β_w are the acoustic pressure, acoustic wavelength, volume of the particle, density of the particle, density of the fluid, compressibility of the particle, and compressibility of the fluid, respectively. In our sorter design, the two sets of FIDTs are symmetric about the O-axis. The phases of coherent signals are modulated so that the SSAW pressure nodes are distributed on the O-axis. The O-axis is aligned with the collection outlet in the Y direction. When cells/particles are injected into the channel, they are focused by two sheath flows. By controlling the two sheath flow rates, those cells/particles enter the waste outlet. As soon as the RF signals are applied to the FIDTs, SSAW is established on the substrate. As a result, the cells/particles in the SSAW area experience the acoustic radiation force and are pushed to the nearest pressure node, entering into the collection outlet.

The performance of SSAW-based sorter is characterized by throughput and sorting rate. The throughput is the total number of cells/particles passing through the device per second, while the sorting rate is defined as the maximum number of sorted events per second. In order to continuously sort individual cells/particles without errors, one and only one particle/cell is allowed in the SSAW area at any given time.³⁷ Therefore, the distance between each cell/particle should be larger than L , where L is the width of SSAW actuation area. When the cells/particles flow through the channel at a constant velocity v , $T_r = L/v$ is the time during which one cell/particle passes through the SSAW area. The maximum throughput could be expressed in terms as:

$$\text{Throughput} = \frac{1}{T_r} = \frac{v}{L} \quad (3)$$

In other words, the width of SSAW area indicates the resolution of sorter, while the combination of SSAW resolution and particle velocity determines the throughput. Moving the particles from one position to another requires a threshold value of impulse I which is:

$$I = F_r \cdot T_{pulse} \quad (4)$$

where T_{pulse} is the width of sorting signal, and it should satisfy $T_{pulse} \leq T_r$. T_{pulse} represents the actual interaction time between cells/particles and SSAW. Thus, the sorting rate can be expressed as $1/T_{pulse}$. Improvements in acoustic sorting throughput require reductions to both the width of the SSAW area (L), and the width of the sorting signal (T_{pulse}). For the SIDTs design, as

these parameters are reduced, so is the energy intensity of the SAW. As a result, there is a limitation on the minimal width of the SSAW area and width of sorting signal, below which the acoustic forces will be insufficient to push cells/particles from their streamlines.

Based on the analysis, we designed the FIDTs structure for high-throughput sorting; as it can provide higher intensity and higher resolution than SIDTs. In analogous to focusing a light beam with an optical lens, the concentric circular-shaped FIDTs generate SAW with a circular wavefront and each wave propagates along the direction to the focal point O. Because of the deformation of wavefront caused by the anisotropy of the substrate, the SAW could not be tightly focused as a small spot at point O. The width of the beam decreases to a certain value and maintains at that value for further propagation.⁵¹ Because the beam is concentrated, the density of acoustic intensity increases. By introducing another focused SAW which is propagating in the opposite direction, SSAW with high resolution and high intensity is generated.

Methods

Device fabrication

The FIDTs were fabricated on a 128° Y-cut, X-propagating lithium niobate (LiNbO₃) substrate. The geometries of FIDTs were fabricated by standard photolithography process and then two thin metal layers (Cr/Au, 5 nm/50 nm) were deposited through an e-beam evaporation (Semicore Corp, USA).⁵² After a lift-off process, two sets of FIDTs formed on the substrate. Each of the FIDTs has 13 pairs of electrodes and the radius R is 500 μm . The designed wavelength of the IDTs is 100 μm at a resonant frequency of 38.8 MHz. Markers were deposited on the substrate for polydimethylsiloxane (PDMS) channel alignment. The PDMS channel fabricated by soft lithography was bonded to the substrate after plasma treatment.

Preparation of particles and cells

For particle patterning and sorting, polystyrene particles

(Bangs Laboratories, USA) with a diameter of 10 μm were suspended in 0.5% sodium dodecyl sulfate (SDS) water solution as sample. The sheath flow buffer was also 0.5% SDS water solution. The different concentration of particles were prepared for patterning and sorting purposes.

HeLa cells (ATCC, CCL-2, USA) were cultured using Dulbecco's Modification of Eagle's Medium (DMEM)/Ham's F-12 50/50 Mix supplemented with 10% FBS and 1% penicillin-streptomycin solution in a 37 °C cell culture incubator. Before the sorting experiment, cells were fixed in 4% formaldehyde/1xPBS solution for 30 minutes. Then the fixed cells were centrifuged and re-suspended with 1x PBS to the desired concentration (2×10^6 cells per mL). The sheath flow buffer was 1x PBS solution.

System setup

The experiments were conducted on the stage of an inverted microscope (TE2000U Nikon, Japan). A high-speed camera (SA4, Photron, Japan) and a CCD camera (CoolSNAP HQ2, Photometrics, USA) were used to record the particle and cell sorting processes. Syringe pumps (NeMESYS, Cetoni GmbH, Germany) were used to inject the sample and to control the flow rate of sample and buffer solution. The SSAW was excited by applying two coherent RF signals on the two sets of FIDTs, respectively. The RF signals were generated by a signal generator (E4422B Agilent, USA) and amplified by a power amplifier (100A250A, Amplifier Research, USA). The microscopic images were processed with an image processing software (ImageJ, NIH, USA).

The width of SSAW area

To compare the acoustic forces and the effective width of SSAW area in microfluidic channels, 10 μm polystyrene particles were employed to visualize the acoustic field. A high-concentration (10^8 particles/ml) solution of polystyrene particles was loaded into a microfluidic channel. These particles were uniformly distributed in the channel and remained stationary. RF signals with a frequency of 38.8 MHz were applied to interdigital transducers (IDTs) to generate SSAW. At the beginning, the

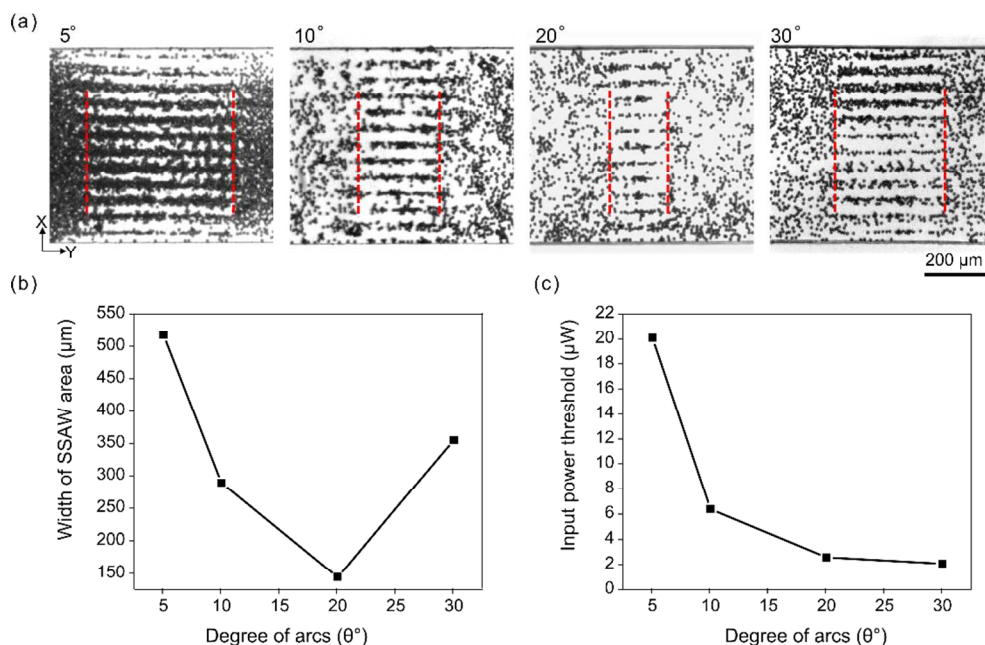


Fig. 2 (a) Particles pattern images. These particles were patterned by FIDTs with different arcs degree at their input power thresholds, respectively. The degree of arcs are 5°, 10°, 20°, and 30°. (b) The width of SSAW area and (c) the input power thresholds are plotted versus the degree of FIDTs.

input power was controlled at a very low level so that the acoustic radiation force was too weak to pattern these particles in channel. Then we gradually increased the input power until the particles showed a clear pattern, as shown in Fig. 2(a) and Fig. 3(a). We defined the input power value as the input power threshold required for static particle patterning. Meanwhile, we estimated the width of the SSAW area by measuring the patterning length in the Y directions. Wide microfluidic channels (600 μm in Fig. 2(a) and 400 μm in Fig. 3(a)) were used to avoid the effect of channel walls on the measurement.

Shift of particles

10 μm polystyrene particles were focused by sheath flow and passed through the SSAW area at a given velocity. Because of the acoustic radiation force, particles were shifted a distance in X direction. The process was recorded by a high-speed camera and the trajectory of particles was obtained by stacking the frames using ImageJ, as shown in Fig. 4(a). The shift of particles was extracted from the trajectory. In the experiment, the IDTs were actuated by continuous RF signal so that the interaction time between SSAW and particles is equal to T_r .

Periodically sorting of particles and cells

To continuously sort cells/particles with high resolution, periodic pulse signals with a repeatability of 200 Hz were applied to the SSAW sorter. The cell/particle presented in the SSAW area during each pulse signal width was sorted while the others were not. In order to sort cells/particles without any error (more than one cell/particle were sorted at once), our experiment requires that only one cell/particle presents in the SSAW actuation area when the acoustic field is applied. Since the distance between each particle varies according to Poisson distribution, we used low concentration of cell samples to minimize the sorting error. By adjusting the input power and pulse width T_{pulse} of RF signal, sorting one particle by each pulse can be achieved in a short period (~ 100 ms).

Numerical simulation

To simulate the SAW generated by different IDT designs, a piezoelectric device module in COMSOL 4.3a (COMSOL Inc., USA) was built and solved at frequency domain. The dimension of the LiNbO_3 substrate for simulations was 3.6 mm \times 1.4 mm \times 0.2 mm (L \times W \times H). The IDTs in the simulation had the same size as the experimental device, except that only 8 pairs of IDT fingers were included. Since the IDTs were symmetrically patterned on the substrate along both the X and Y directions, only a quarter of the substrate was modeled to improve the computation efficiency. The properties of the substrate were given at the crystal orientation of 128° Y-cut and SAW propagated along the X orientation of the substrate. A RF signal with a power intensity of 1 W was applied to the IDTs while other boundaries were set as zero charge. The bottom of the substrate was fixed constraint to mimic the experimental conditions. A frequency scan was carried out for each IDTs' design to identify the resonant frequency. Each design resonated at around 38.8 MHz, which is well agreed with experiments.

Results and discussion

Optimization of FIDTs

In order to achieve the highest performance of FIDTs, the design parameters of FIDTs need to be optimized. To date, there is still no systematic study on the properties of SSAW generated by FIDTs under different design parameters. Therefore we compared

several design parameters to find out the optimum design of FIDTs for the cell sorting application.

The target of the optimization is to find the best design combination that can generate the narrowest beam width of SSAW area. The narrower the beam width, the higher the theoretical throughput can be achieved. There are two major parameters that may influence the beam width of the SSAW area, the FIDTs' arc degree θ , and the geometric focal length R .⁵³ We first studied the effects of different focal length R on the actual beam width. As shown in Fig. S1 (Supporting Information), the actual beam width increases slightly as the increase of R . The difference in the actual beam width is rather insignificant among different R values (from 500 μm to 2000 μm). The result is not surprising as our design establishes a standing wave field, which allows uniform energy distribution of acoustic waves between the two sets of FIDTs. Since we determined that R is not a critical parameter influencing the sorting performance, we choose $R=500$ μm considering the balance between the device footprint and the propagation loss of acoustic waves.

Under the same R (500 μm), we also compared the beam width of the SSAW area with different degrees of arc θ . Four arc degree θ (5° , 10° , 20° , and 30°) were studied in this work. We used 10 μm polystyrene particles to visualize the beam width of the SSAW area. The width of the SSAW area was measured at the input power thresholds (the minimum power input required to form the pattern); as shown in Fig. 2(a). Fig. 2(b) shows that the beam width of the SSAW area is minimum when θ is 20° . Theoretically, the beam compression ratio (original beam width to minimum beam width) becomes larger as θ increases.³⁷ However, our experimental results showed that a higher beam compression ratio does not definitely result in a smaller beam width. The actual beam width is a combined result of beam compression ratio and original beam width. A larger θ (e.g., 30°)

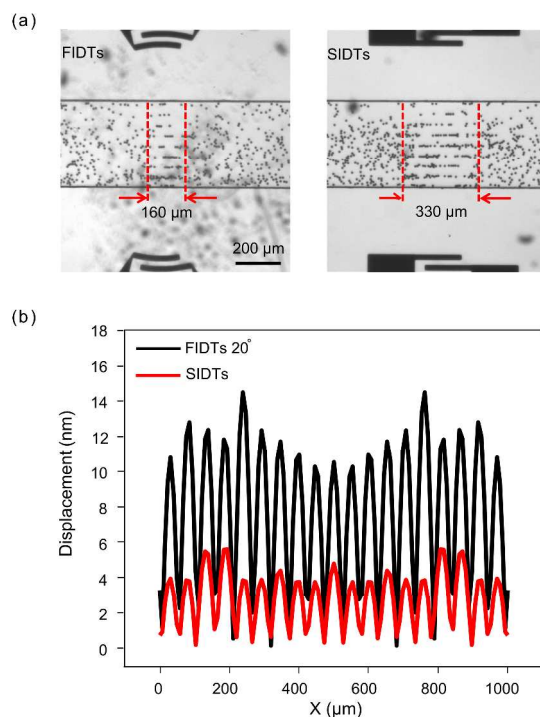


Fig. 3 (a) Images of SSAW based particle patterning. These particles were patterned by FIDTs (Left) and SIDTs (Right) at their input power thresholds, respectively. (b) The numerically simulated displacements along X axis between two sets of IDTs are compared. The displacement of FIDTs (black line) is 2–3 times larger than that of SIDTs (red line). The displacements distribute uniformly along X axis.

will generate a larger original beam width. Therefore, the actual beam width is still larger than the smaller θ (20°), even if the larger θ has a higher beam compression ratio. Moreover, the deformation and dispersion of the surface acoustic wavefront owing to the anisotropic property of the substrate become significant when the degree of arcs θ get larger. We also found that the power threshold decreases along with the increase of θ , indicating that FIDTs with larger arcs have better energy efficiency (Fig. 2(c)). Collectively, the 20° FIDTs were used as the optimal condition due to the highest spatial resolution and good energy efficiency.

Comparison of FIDTs and SIDTs

As discussed in the Mechanism section, FIDTs are expected to have better resolution and produce stronger acoustic radiation forces than conventional SIDTs. With SIDTs, it is difficult to generate a narrow beam width L because the finite aperture of the SIDTs causes the diffraction of SAW, resulting in a curved wavefront rather than the desired flat one, especially when the resonant wavelength is similar to the aperture.⁵⁴

With the optimized FIDTs design, we compared the performance between FIDTs and SIDTs to quantify the advantages of FIDTs. The optimal FIDTs design ($R=500\ \mu\text{m}$; $\theta=20^\circ$) was used for the comparison. The width of SIDTs (*i.e.*,

aperture of SIDTs) was set to be $175\ \mu\text{m}$, which is equal to the length of the shortest arc in FIDTs. The same patterning method described in the previous section was used to compare the beam width generated by SIDTs and FIDTs. Fig. 3(a) shows the images of particles patterned by the two kinds of IDTs at their input power thresholds, respectively. The width of SSAW area for SIDTs ($\sim 330\ \mu\text{m}$) is larger than its aperture ($175\ \mu\text{m}$) and is around two times of the one for FIDTs ($\sim 160\ \mu\text{m}$), indicating that the diffraction of the SSAW is effectively suppressed by the FIDTs structure.

After showing that FIDTs can generate much smaller beam width, we further studied the amplitude of acoustic radiation forces generated by these two types of IDTs. The comparison of acoustic radiation forces between the two types of IDTs was carried out through both 3D numerical simulation and experimental measurement. Fig. 3(b) shows the simulated substrate surface displacement of FIDTs (black line) and SIDTs (red line) using a COMSOL model (Fig. S2 in the Supporting Information). The FIDTs show larger surface displacement than SIDTs under the same input power due to concentration of acoustic waves. The displacement of FIDTs is 2–3 times larger than that of SIDTs. The acoustic pressure p_0 is directly proportional to the displacement of the surface d . According to equation (1), we have:

$$F_r \propto d^2 \quad (5)$$

Therefore, a 2–3 times higher displacement can be translated to a 4–9 times higher acoustic radiation force generated by FIDTs than SIDTs.

We also examined the enhanced acoustic radiation force generated by the FIDTs experimentally. To quantify the comparisons, we measured the lateral shift of particles when they flow through the SSAW area of FIDTs and SIDTs, respectively. Fig. 4(a) shows the particle trajectory in the microfluidic channel when the FIDTs are on. Different input powers were applied while the travelling velocity of particles were kept a constant value of $0.1\ \text{m/s}$. Fig. 4(b) shows the relationship between the input power and the shift of particles in the X direction for the two types of IDTs. The shift increased with an increase in input power and reached its maximum value when the particle arrived at the pressure node. The minimum input power that could move particles to the pressure node was around $1.6\ \text{mW}$ for FIDTs (red circle), while this value was around $15\ \text{mW}$ for SIDTs (black square), which means the FIDTs could generate the same sorting effect as SIDTs while only required $1/9$ of the input power. Based on the theoretical and experimental results, the energy efficiency of SSAW generated by FIDTs is much higher compared to that of SIDTs. It should be noted that the maximum shift of particles for FIDTs is a little larger, because the pressure nodes of FIDTs and SIDTs were slightly misaligned. The deformation of PDMS channel under high input power is another possible reason that causes this measurement error.

Particle sorting under different flow velocities

Thus far, we have demonstrated that our FIDTs design possesses the capability to sort cells/particles with a higher resolution and higher energy efficiency than SIDTs. Eq. (4) indicates that the velocity of particles affects the sorting ability by determining the time T_r . As particle velocity increases, the input power required to sort particles also increases. However, there is an upper limit on the input power that can be applied to the substrate before the substrate is damaged or cracked. This limitation on the maximum input power thereby limits the highest possible sorting throughput of SSAW-based devices.

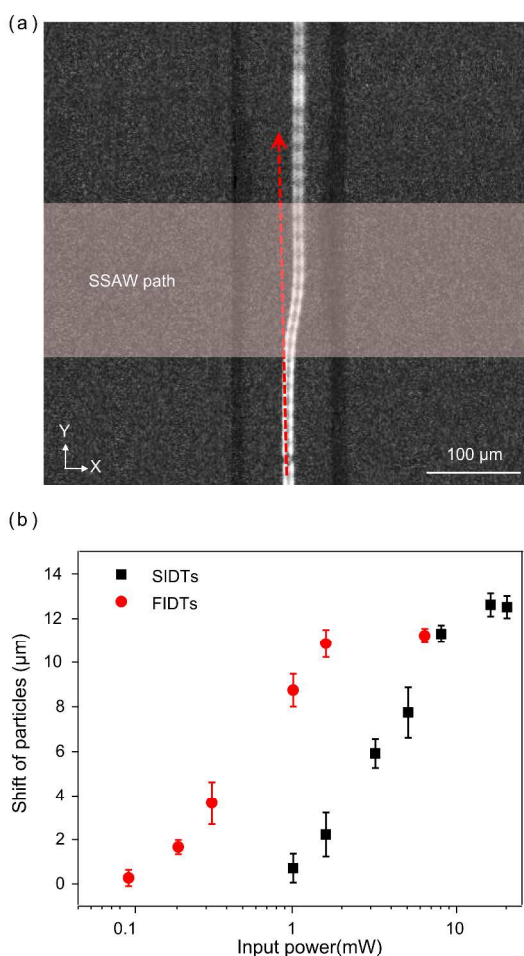


Fig. 4 (a) The particle trajectory in the microfluidic channel when the FIDTs are on. (b) Comparison of the shift in particle position in the X direction caused by FIDTs (red circle) and SIDTs (black square). The FIDTs show higher energy efficiency than SIDTs. The required input power for FIDTs is around 9 times less than SIDTs when the particles are pushed to the pressure node.

To investigate the performance of our device for sorting particles with different velocities, polystyrene particles with three different velocities (0.14, 0.25, and 0.34 m/s) flowed through the SSAW area while the input power changed from 0.3 mW to 12.6 mW.

The sorting performance was characterized by measuring the X-direction shift of particles. The experimental results in Fig. 5 shows that the slower particles move a longer distance in the X direction under the same input power because they experience longer T_p . For the highest velocity of 0.34 m/s in our experiment, the input power required to deflect particles from their initial line to the pressure node is around 10 mW.

High-throughput sorting of particles and cells

After optimizing the design parameters and confirming the basic functions of our FIDT based high-throughput SSAW device, we examined its sorting capability. We first performed sorting of 10 μm polystyrene particles using the FIDT device. The polystyrene particles were loaded into the sorting device at a velocity of 0.25 m/s. Once the flow is stable, a periodical RF signal was applied to the FIDTs. As shown in Fig. 6(a), our sorter can effectively sort out a single particle (Particle 2) from its neighboring particles (Particles 1 and 3) by adjusting the input power and pulse width T_{pulse} of the RF signal. After passing through the SSAW actuation area and being exposed to the acoustic radiation force, all particles (particles 1, 2, and 3) were affected by the SSAW beam and shifted away from the initial focused line. However, only the shift of particle 2, which is in the middle position of SSAW area, was large enough to meet the conditions to be sorted. Here, the input power was 31.6 mW, and T_{pulse} was 72 μs . The 72 μs

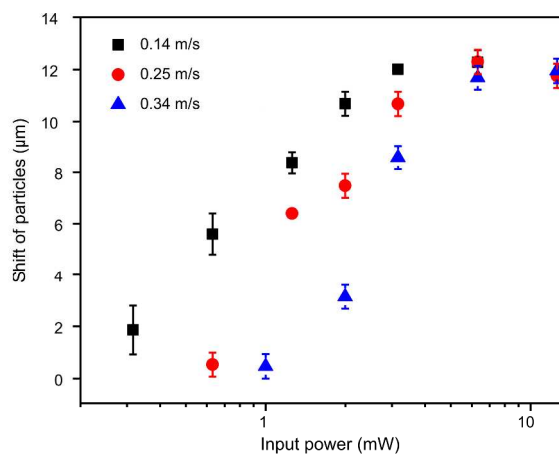


Fig. 5 The relationship between the velocity of particles and their position shift caused by FIDTs. The three flow velocities are 0.14 m/s, 0.25 m/s, and 0.34 m/s, respectively.

actuation time means that the theoretical maximum sorting rate can be as high as 13,800 events/s for polystyrene particles. For actual throughput, it is also dependent on the concentration of the sample. In this case, the concentration of polystyrene particles allows a throughput of 3,300 events/s at the particle velocity of 0.25 m/s. It is worth noting that the distance between particles, which is around 76 μm under such concentration, is shorter than the SSAW beam width of 160 μm obtained in Fig. 3(a). The particles only move forward a distance of 18 μm during the T_{pulse} . It means at least one of the particles 1 and 3 was in the SSAW

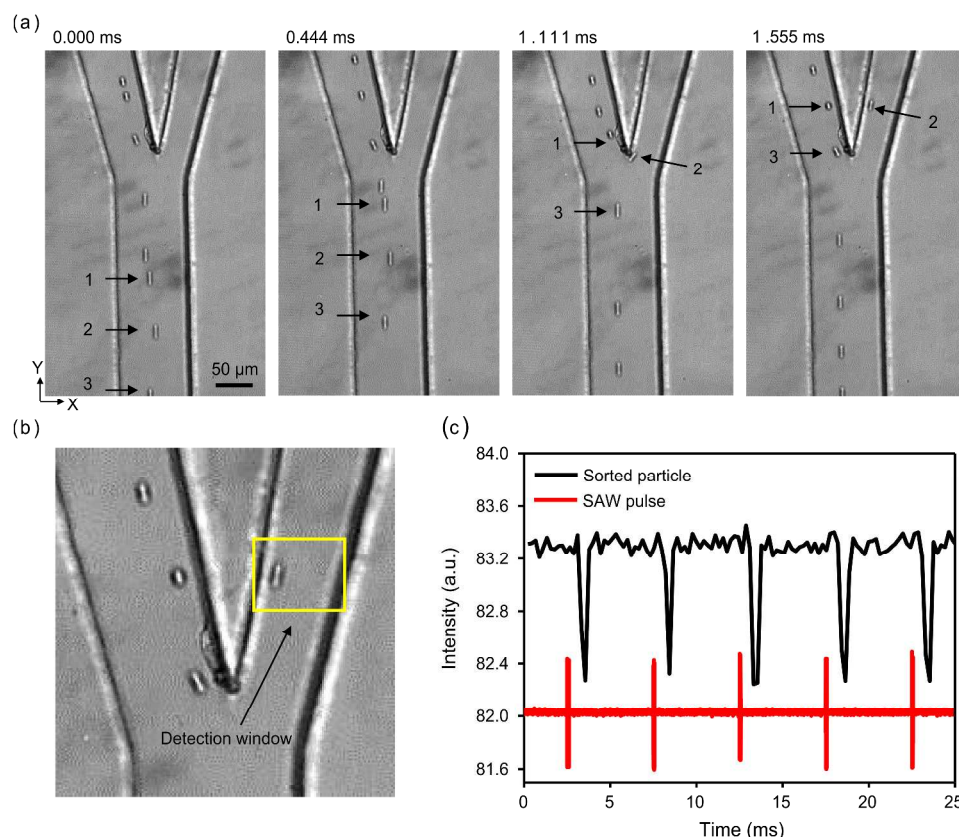


Fig. 6 (a) The time-lapse images of individual particle sorting event. After experiencing the SSAW, particle 2 was pushed out from the initial line and entered the collection outlet. (b) The grayscale intensity value in the detection window of each frame was extracted using ImageJ and (c) the change of intensity is plotted versus time. Every dip in the intensity (black) indicates a particle passing through the detection window. The pulse signal with a repeatability of 200 Hz is also plotted (red). Every intensity dip exactly follows a signal pulse. It proves that the particle is sorted by SSAW.

area during that time. However, the shifts of particles 1 and 3 were far less than that of particle 2. It is thus reasonable to assume that the acoustic intensity of the SSAW area has a peak-shape distribution along the Y axis. By controlling the input power, we could realize an effective width of SSAW area shorter than 160 μm .

In order to prove that the particle was sorted by acoustic radiation force instead of imperfect particle focusing or flow instability, we also examined the reproducibility of this sorting process. The experimental video (Supplementary Movie 1) was analyzed by setting a detection window indicated in Fig. 6(b). The grayscale intensity value in the window area was extracted for each frame through ImageJ. When a particle is present in the window, the gray-level intensity decreases and shows as a dip in the intensity line. In Fig. 6(c), the frame intensity (black), as well as the pulse signal (red), was plotted versus time. Each dip of the intensity exactly follows a pulse signal. Each pulse signal could sort one single particle precisely.

After demonstrating that our device can achieve a throughput of 3,300 events/s for particle sorting, we also applied our device to sort mammalian cells. Here, we used HeLa cells as the mammalian cell model to validate the performance of our device. Similar experimental procedures were followed as the particle-sorting experiment. As shown in Fig. 7, when the sorter was off, all of the cells were hydrodynamically guided into the top outlet. Once the pulse signal was triggered, the target cell (blue dashed circle) was exposed to the acoustic field (red shadow) and deflected. The acoustic field only impacted a small region and disappeared instantaneously when the pulse signal finished so that only the target cell was sorted into the bottom outlet.

Compared with the sorting of polystyrene particles, we used

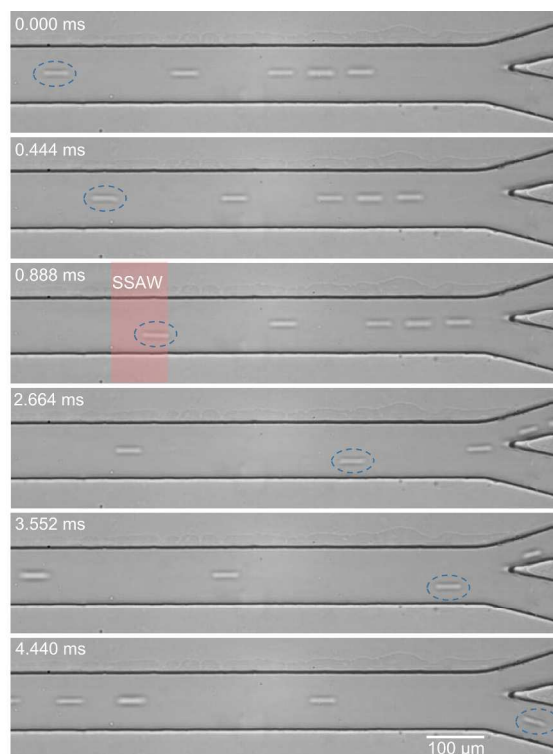


Fig. 7 The time-lapse images of individual HeLa cell sorting event. HeLa cells travel through the channel and enter the top outlet when the sorter is off. The SSAW field (red shadow) is established when the sorter is on. Only the target cell (blue dashed circle) which is in the SSAW field is deflected, entering the bottom outlet.

longer pulse signal width T_{pulse} (144 μs) and higher input power (63.1 mW) to sort HeLa cells. Since cells are more difficult to be densely packed due to aggregation,²⁴ the possibility that cells presented in sorting area during the pulse width is low. The longer pulse width and higher input power used here allow successful cell sorting in our experiment. Based on the pulse signal width T_{pulse} (144 μs), the sorting rate for HeLa cells is calculated to be $\sim 7,000$ cells/s.

Conclusion

In this work, we present a high-throughput SSAW cell/particle sorter. Instead of using standard parallel IDTs to generate SSAW, we designed two sets of FIDTs to generate a narrow and intense SSAW beam for sorting of cells/particles. The high spatial resolution and high energy efficiency were demonstrated through experiments and numerical simulations. Our device archived an actual sorting throughput of 3,300 events/s. Under an input power of 31.6 mW (15 dBm), we demonstrated that an actuation time T_{pulse} of 72 μs is long enough to sort one particle, which indicates a potential sorting rate as high as $\sim 13,800$ events/s. By precisely controlling the input power applied to the FIDTs, our device has potential to sort particles into multiple channels. It overcomes the limitation of conventional IDTs designs and improves the performance of acoustic cell sorters.

Although we have demonstrated the high throughput and sorting rate, the performance of current devices could be further improved by incorporating a cell-detection unit. Currently, since our SSAW cell sorter lacks the cell-detection unit, the timing of the acoustic trigger can hardly match the position of particles/cells in our cell-sorting experiments. Particles/cells might be out of the optimized actuation area when the acoustic cell-sorting unit was activated, thereby requiring a longer sorting pulse or higher sorting power for successful sorting. By integrating our acoustic cell-sorting unit with an optical cell-detection unit^{55–58}, the input power and pulse width can be further decreased and a throughput of $\sim 10,000$ events/s should be within reach. With further improvement, our high-throughput SSAW cell sorter provides a promising platform for development of high-performance, low-cost, on-chip FACS.

Acknowledgements

We gratefully acknowledge financial support from National Institutes of Health (1 R01 GM112048-01A1 and 1R33EB019785-01), National Science Foundation (IIP-1534645 and IDBR-1455658), and the Penn State Center for Nanoscale Science (MRSEC) under grant DMR-1420620. J.P.M. and S.J.L. are supported by the NHLBI Division of Intramural Research. Components of this work were conducted at the Penn State node of the NSF-funded National Nanotechnology Infrastructure Network. We also acknowledge the Research Computing and Cyberinfrastructure Unit of Information Technology Services at The Pennsylvania State University for providing advanced computing resources and services that have contributed to the research results reported in this paper.

^a Department of Engineering Science and Mechanics, The Pennsylvania State University, University Park, PA 16802, USA.

^b Ascent Bio-Nano Technologies, Inc., State College, PA, 16802, USA

^c National Heart, Lung, and Blood Institute (NHLBI), NIH, Bethesda, MD, USA

[†] The authors contributed equally to this work.

*To whom correspondence should be addressed: junhuang@psu.edu

References

- 1 H. M. Davey and D. B. Kell, *Microbiol. Rev.*, 1996, **60**, 641–696.
- 2 M. Eisenstein, *Nature*, 2006, **441**, 1179–1185.
- 3 H. M. Shapiro, *Practical Flow Cytometry*, Wiley-Liss, 4th edn., 2003.
- 4 J. F. Leary, *Cytometry. A*, 2005, **67**, 76–85.
- 5 F. Guo, X.-H. Ji, K. Liu, R.-X. He, L.-B. Zhao, Z.-X. Guo, W. Liu, S.-S. Guo and X.-Z. Zhao, *Appl. Phys. Lett.*, 2010, **96**, 193701.
- 6 H.-S. Moon, K. Kwon, S.-I. Kim, H. Han, J. Sohn, S. Lee and H.-I. Jung, *Lab Chip*, 2011, **11**, 1118–1125.
- 7 J. Sun, Y. Gao, R. J. Isaacs, K. C. Boelte, P. C. Lin, E. M. Boczek and D. Li, *Anal. Chem.*, 2012, **84**, 2017–2024.
- 8 M. P. MacDonald, G. C. Spalding and K. Dholakia, *Nature*, 2003, **426**, 421–424.
- 9 X. Wang, S. Chen, M. Kong, Z. Wang, K. D. Costa, R. A. Li and D. Sun, *Lab Chip*, 2011, **11**, 3656–3662.
- 10 Y. Chen, A. J. Chung, T.-H. Wu, M. A. Teitell, D. Di Carlo and P.-Y. Chiou, *Small*, 2014, **10**, 1746–1751.
- 11 Y. Chen, T.-H. Wu, Y.-C. Kung, M. A. Teitell and P.-Y. Chiou, *Analyst*, 2013, **138**, 7308–7315.
- 12 B. D. Plouffe, M. Mahalanabis, L. H. Lewis, C. M. Klapperich and S. K. Murthy, *Anal. Chem.*, 2012, **84**, 1336–1344.
- 13 J. Wang, K. Morabito, T. Erkers and A. Tripathi, *Analyst*, 2013, **138**, 6573–6581.
- 14 D. Di Carlo, D. Irimia, R. G. Tompkins and M. Toner, *Proc. Natl. Acad. Sci. U. S. A.*, 2007, **104**, 18892–18897.
- 15 A. Y. Fu, H.-P. Chou, C. Spence, F. H. Arnold and S. R. Quake, *Anal. Chem.*, 2002, **74**, 2451–2457.
- 16 J. Shi, S. Yazdi, S.-C. S. Lin, X. Ding, I.-K. Chiang, K. Sharp and T. J. Huang, *Lab Chip*, 2011, **11**, 2319–2324.
- 17 J. Shi, H. Huang, Z. Stratton, Y. Huang and T. J. Huang, *Lab Chip*, 2009, **9**, 3354–3359.
- 18 M. Wiklund and H. M. Hertz, *Lab Chip*, 2006, **6**, 1279–1292.
- 19 X. Ding, S.-C. S. Lin, B. Kiraly, H. Yue, S. Li, I.-K. Chiang, J. Shi, S. J. Benkovic and T. J. Huang, *Proc. Natl. Acad. Sci. U. S. A.*, 2012, **109**, 11105–11109.
- 20 X. Ding, Z. Peng, S.-C. S. Lin, M. Geri, S. Li, P. Li, Y. Chen, M. Dao, S. Suresh and T. J. Huang, *Proc. Natl. Acad. Sci. U. S. A.*, 2014, **111**, 12992–12997.
- 21 P. Li, Z. Mao, Z. Peng, L. Zhou, Y. Chen, P.-H. Huang, C. I. Truica, J. J. Drabick, W. S. El-Deiry, M. Dao, S. Suresh and T. J. Huang, *Proc. Natl. Acad. Sci. U. S. A.*, 2015, **112**, 4970–4975.
- 22 Y. Chen, A. A. Nawaz, Y. Zhao, P.-H. Huang, J. P. McCoy, S. J. Levine, L. Wang and T. J. Huang, *Lab Chip*, 2014, **14**, 916–923.
- 23 H. Mulvana, S. Cochran and M. Hill, *Adv. Drug Deliv. Rev.*, 2013, **65**, 1600–1610.
- 24 J. S. Jeong, J. W. Lee, C. Y. Lee, S. Y. Teh, A. Lee and K. K. Shung, *Biomed. Microdevices*, 2011, **13**, 779–788.
- 25 Y. Chen, S. Li, Y. Gu, P. Li, X. Ding, L. Wang, J. P. McCoy, S. J. Levine and T. J. Huang, *Lab Chip*, 2014, **14**, 924–930.
- 26 J. Xu and D. Attinger, *J. Micromechanics Microengineering*, 2008, **18**, 065020.
- 27 G. Yu, X. Chen and J. Xu, *Soft Matter*, 2011, **7**, 10063.
- 28 F. Guo, P. Li, J. B. French, Z. Mao, H. Zhao, S. Li, N. Nama, J. R. Fick, S. J. Benkovic and T. J. Huang, *Proc. Natl. Acad. Sci. U. S. A.*, 2015, **112**, 43–48.
- 29 J. Hultström, O. Manneberg, K. Dopf, H. M. Hertz, H. Brismar and M. Wiklund, *Ultrasound Med. Biol.*, 2007, **33**, 145–151.
- 30 D. L. Miller, N. B. Smith, M. R. Bailey, G. J. Czarnota, K. Hynynen and I. R. S. Makin, *J. Ultrasound Med.*, 2012, **31**, 623–634.
- 31 L. Johansson, F. Nikolajeff, S. Johansson and S. Thorslund, *Anal. Chem.*, 2009, **81**, 5188–5196.
- 32 C. Lee, J. Lee, H. H. Kim, S.-Y. Teh, A. Lee, I.-Y. Chung, J. Y. Park and K. K. Shung, *Lab Chip*, 2012, **12**, 2736–2742.
- 33 O. Jakobsson, C. Grenvall, M. Nordin, M. Evander and T. Laurell, *Lab Chip*, 2014, **14**, 1943–1950.
- 34 The Beckman Coulter, <http://www.beckmancoulter.com/>.
- 35 S.-C. S. Lin, X. Mao and T. J. Huang, *Lab Chip*, 2012, **12**, 2766–2770.
- 36 X. Ding, P. Li, S.-C. S. Lin, Z. S. Stratton, N. Nama, F. Guo, D. Slotcavage, X. Mao, J. Shi, F. Costanzo and T. J. Huang, *Lab Chip*, 2013, **13**, 3626–3649.
- 37 T. Franke, S. Braunmüller, L. Schmid, A. Wixforth and D. a Weitz, *Lab Chip*, 2010, **10**, 789–794.
- 38 L. Schmid, D. A. Weitz and T. Franke, *Lab Chip*, 2014, **14**, 3710–3718.
- 39 X. Ding, S.-C. S. Lin, M. I. Lapsley, S. Li, X. Guo, C. Y. Chan, I.-K. Chiang, L. Wang, J. P. McCoy and T. J. Huang, *Lab Chip*, 2012, **12**, 4228–4231.
- 40 X. Ding, J. Shi, S.-C. S. Lin, S. Yazdi, B. Kiraly and T. J. Huang, *Lab Chip*, 2012, **12**, 2491–2497.
- 41 S. Li, X. Ding, F. Guo, Y. Chen, M. I. Lapsley, S.-C. S. Lin, L. Wang, J. P. McCoy, C. E. Cameron and T. J. Huang, *Anal. Chem.*, 2013, **85**, 5468–5474.
- 42 S. K. R. S. Sankaranarayanan and V. R. Bhethanabotla, *IEEE Trans. Ultrason. Ferroelectr. Freq. Control*, 2009, **56**, 631–643.
- 43 R. Shilton, M. K. Tan, L. Y. Yeo and J. R. Friend, *J. Appl. Phys.*, 2008, **104**, 014910.
- 44 M. K. Tan, J. R. Friend and L. Y. Yeo, *Phys. Rev. Lett.*, 2009, **103**, 024501.
- 45 G. Destgeer, K. H. Lee, J. H. Jung, A. Alazzam and H. J. Sung, *Lab Chip*, 2013, **13**, 4210–4216.
- 46 G. Destgeer, S. Im, B. Hang Ha, J. Ho Jung, M. Ahmad Ansari and H. Jin Sung, *Appl. Phys. Lett.*, 2014, **104**, 023506.
- 47 M. Sesen, T. Alan and A. Neild, *Lab Chip*, 2014, **14**, 3325–3333.
- 48 J. Shi, X. Mao, D. Ahmed, A. Colletti and T. J. Huang, *Lab Chip*, 2008, **8**, 221–223.
- 49 K. Yosioka and Y. Kawasima, *Acta Acust. united with Acust.*, 1955, **5**, 167–173(7).
- 50 A. Nilsson, F. Petersson, H. Jönsson and T. Laurell, *Lab Chip*, 2004, **4**, 131–135.
- 51 S. R. Fang and S. Y. Zhang, *IEEE Trans. Ultrason. Ferroelect. Freq. Contr.*, 1989, **36**, 178–184.
- 52 J. Shi, D. Ahmed, X. Mao, S.-C. S. Lin, A. Lawit and T. J. Huang, *Lab Chip*, 2009, **9**, 2890–2895.
- 53 T. Wu, H. Tang, Y. Chen and P. Liu, *IEEE Trans. Ultrason. Ferroelect. Freq. Contr.*, 2005, **52**, 1384–1392.
- 54 O. Tigli and M. E. Zaghoul, *IEEE Sens. J.*, 2008, **8**, 1807–1815.
- 55 Y. Zhao, Z. S. Stratton, F. Guo, M. I. Lapsley, C. Y. Chan, S.-C. S. Lin and T. J. Huang, *Lab Chip*, 2013, **13**, 17–24.

-
- 56 X. Mao, A. A. Nawaz, S.-C. S. Lin, M. I. Lapsley, Y. Zhao, J. P. McCoy, W. S. El-Deiry and T. J. Huang, *Biomicrofluidics*, 2012, **6**, 24113–241139.
- 57 C. Zhao, Y. Liu, Y. Zhao, N. Fang and T. J. Huang, *Nat. Commun.*, 2013, **4**, 2305.
- 58 Y. Zhao, S.-C. S. Lin, A. A. Nawaz, B. Kiraly, Q. Hao, Y. Liu and T. J. Huang, *Opt. Express*, 2010, **18**, 23458–23465.

10